


Influence of the triangular Mn-O breathing mode on magnetic ordering in multiferroic hexagonal manganites

Tara N. Tošić^{1,*}, Quintin N. Meier^{2,1} and Nicola A. Spaldin¹

¹Materials Theory, ETH Zürich, Wolfgang-Pauli-Strasse 27, 8093 Zurich, Switzerland

²Université Grenoble Alpes, CEA, LITEN, 17 rue des Martyrs, 38054 Grenoble, France

 (Received 8 March 2022; revised 29 June 2022; accepted 2 August 2022; published 13 September 2022)

We use a combination of symmetry analysis, phenomenological modeling, and first-principles density functional theory to explore the interplay between the magnetic ground state and the detailed atomic structure in the hexagonal rare-earth manganites. We find that the magnetic ordering is sensitive to a breathing mode distortion of the Mn and O ions in the ab plane, which is described by the K_1 mode of the high-symmetry structure. Our density functional calculations of the magnetic interactions indicate that this mode particularly affects the single-ion anisotropy and the interplanar symmetric exchanges. By extracting the parameters of a magnetic model Hamiltonian from our first-principles results, we develop a phase diagram to describe the magnetic structure as a function of the anisotropy and exchange interactions. This in turn allows us to explain the dependence of the magnetic ground state on the identity of the rare-earth ion and on the K_1 mode.

DOI: [10.1103/PhysRevResearch.4.033204](https://doi.org/10.1103/PhysRevResearch.4.033204)

I. INTRODUCTION

The hexagonal manganites, h - $RMnO_3$, where $R = \text{In, Sc, Y, and Dy to Lu}$, are a class of multiferroic materials that show a combination of improper ferroelectricity and antiferromagnetism. Their hexagonal symmetry results in almost degenerate free energy surfaces in the hexagonal ab plane for both the improper ferroelectric distortion [1–4] and the magnetic order [1,5,6]. As a consequence of these quasidegenerate ferroelectric and magnetic energy surfaces, small changes in the crystal chemistry lead to different structural and magnetic ground states. For example, in InMnO_3 , small variations in the defect concentration favor either the improper ferroelectric state or a related antipolar phase [7,8]. The magnetic energy surface in hexagonal manganites is even flatter. While all members of the series have a frustrated in-plane antiferromagnetic (AFM) arrangement of the Mn^{3+} spin magnetic moments, the exact magnetic ground state varies with no obvious trend from compound to compound [9].

The goal of this work is to rationalize the evolution of the magnetic ground state across the hexagonal manganite series. We achieve this by decomposing the structural ground states into their distortions from the high-symmetry prototype structure and determining the effects of these distortions on the magnetic interactions. We show that the magneto-structural coupling is significant, consistent with previous studies on the magnon-phonon coupling in h - $RMnO_3$ [10,11]. Our main

finding is that the crystallographic K_1 mode, which consists of an in-plane triangular inwards or outwards breathing of the Mn and O ions, has a strong effect on the interplanar exchanges and single-ion anisotropies, and ultimately determines the magnetic ground state of each material. Uncovering the details of this particular magneto-structural coupling sets the stage for engineering the magnetic order in this family of compounds.

II. STRUCTURE

The h - $RMnO_3$ structure consists of layers of corner-sharing MnO_5 trigonal bipyramids alternating in the c direction with triangular layers of R -site cations. All members of the series adopt the nonpolar $P6_3/mmc$ space group at high temperature and undergo a structural phase transition at a critical temperature T_c that ranges from 1200–1600 K, depending on the radius of the R site [12,13]. At T_c the crystal symmetry lowers from nonpolar $P6_3/mmc$ to polar $P6_3cm$, with the corresponding structural distortion consisting primarily of a K_3 mode, accompanied by a polar Γ_2^- mode [14], of the high-symmetry structure. An additional smaller structural distortion, corresponding to a K_1 mode, can also occur and has been associated with the onset of magnetic ordering at lower temperature [15,16]. We describe these distortion modes in detail next, reporting their contributions to both the experimentally observed structures and the Landau free energies which we extract using the INVARIANTS software from the group theoretical ISOTROPY Software Suite [17].

A. K_3 and Γ_2^- modes

The primary order parameter driving the structural phase transition at T_c describes a zone boundary mode at $\mathbf{k} = (1/3, 1/3, 0)$, belonging to the K_3 irreducible representa-

*tara.tosic@mat.ethz.ch

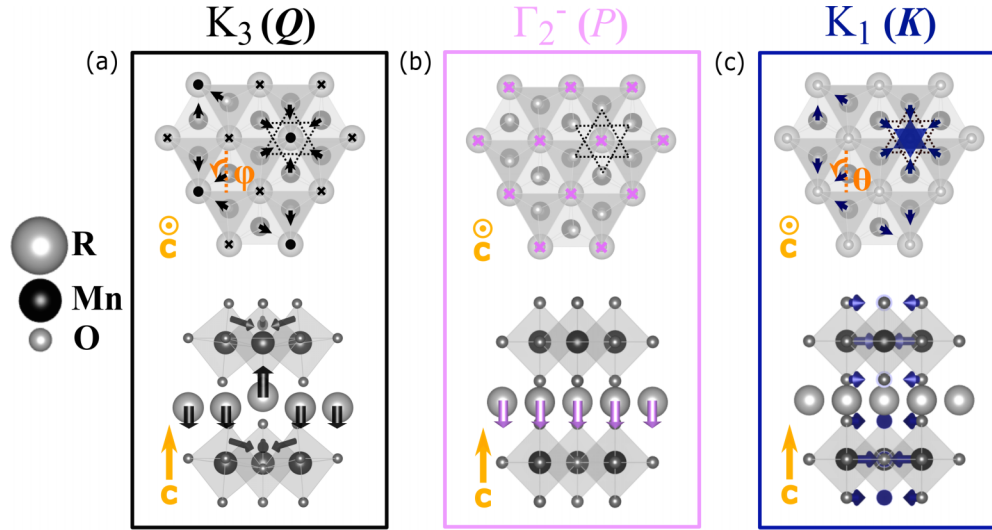


FIG. 1. Structural distortions associated with the coupled K_3 , Γ_2^- , and K_1 modes and their respective order parameters \mathcal{Q} , \mathcal{P} , and \mathcal{K} . (a) $K_3(\mathcal{Q})$. Black arrows represent the buckling of the R ions as well as the direction of the bipyramidal tilts, the latter characterized by the angle ϕ (in this example, $\phi = 2\pi/3$). (b) $\Gamma_2^-(\mathcal{P})$. Pink arrows show the vertical displacement of the R ions associated with a negative polarization along the c axis. Note that displacements of O and Mn sites along c also occur within Γ_2^- but are not represented here. (c) $K_1(\mathcal{K})$. Blue arrows indicate planar Mn and apical O displacements, their direction described by a characteristic angle θ (in the above example, $\theta = 2\pi/3$). Shaded blue triangles show stacked triangular Mn trimers breathing in, relative to the high symmetry position Mn trimers (shown in dotted black lines), as a result of a negative δx_{Mn} displacement.

tion of the high-symmetry $P6_3/mmc$ structure [1,2,4,14]. The distortion, illustrated in Fig. 1(a), consists of triangles of MnO_5 trigonal bipyramids tilting towards or away from their corner-shared O site, accompanied by a buckling of the R -ion plane along the c axis, and results in a trimerization of the lattice. We write the associated primary order parameter as $\mathcal{Q} = \mathcal{Q}(\cos(\phi), \sin(\phi))$, with \mathcal{Q} giving the amplitude of the tilt and the angle ϕ its phase, as illustrated in Fig. 1(a). The tilt angles have sixfold symmetry with $\phi = n\pi/3$ and the integer $n = 1, \dots, 6$. The ferroelectric polarization \mathcal{P} results from a net displacement of the R ions along c belonging to the Γ_2^- irreducible representation of the $P6_3/mmc$ structure. \mathcal{P} emerges through a coupling to \mathcal{Q} , established to be of the form

$$f_{\mathcal{Q}\mathcal{P}} \propto \mathcal{Q}^3 \mathcal{P} \cos(3\phi)$$

to lowest order in the Landau expansion of the free energy [1,2,14].

B. K_1 mode and its coupling to K_3 and Γ_2^-

In addition to the K_3 and the Γ_2^- modes, a third structural distortion is reported at temperatures below T_c , although with much smaller amplitude [16,18–21]; group theoretical analysis of the minimum energy structure of YMnO_3 , calculated using density functional theory (DFT), indicated that its corresponding ionic displacements are one and two orders of magnitude smaller than those of the Γ_2^- and K_3 modes, respectively [14]. The mode belongs to the K_1 irreducible representation of the $P6_3/mmc$ structure at the same $\mathbf{k} = (1/3, 1/3, 0)$ value as K_3 . K_1 involves collective planar displacements of the Mn ions and their apical O (O_{ap}) ions parallel to the directions of the bipyramidal tilts projected onto the ab plane, as depicted in Fig. 1(c). Within this mode, the displacements of the O_{ap} ions are much smaller than

those of the Mn ions [14]. Therefore, K_1 is discussed in terms of displacements δx_{Mn} of the Mn ions away from their high symmetry positions at their Wyckoff site $(1/3, 0, 0)$ [16]. Throughout this work, δx_{Mn} is expressed in units of fractional coordinates of the in-plane lattice parameters. Movements of Mn sites away ($\delta x_{\text{Mn}} > 0$) or towards ($\delta x_{\text{Mn}} < 0$) their corresponding trimerization centers lead to a triangular breathing inwards and outwards of Mn sites that belong to the same trimer, as depicted by the respective contraction and expansion of blue triangles in Fig. 2. The K_1 mode can also be described within the Landau free energy expansion by its order parameter $\mathcal{K} = \mathcal{K}(\cos(\theta); \sin(\theta))$, where θ describes the direction of the Mn and apical O displacements and \mathcal{K} is their amplitude. The K_1 mode is like the Γ_2^- mode in that it is stable in the high symmetry structure and it differs in that it is constrained by a threefold symmetry:

$$f_{\mathcal{K}} = \beta_1 \mathcal{K}^2 + \beta_2 \mathcal{K}^3 \cos(3\theta). \quad (1)$$

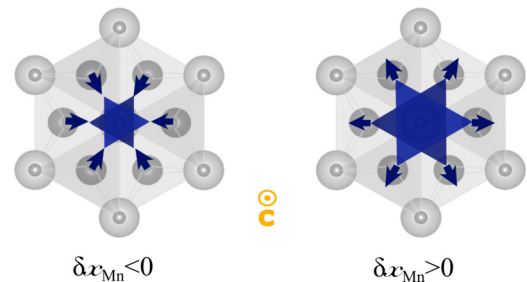


FIG. 2. Planar breathing in (left) and out (right) of Mn sites, corresponding to, respectively, a negative and positive δx_{Mn} displacement within the K_1 mode.

TABLE I. Diffraction measurements of δx_{Mn} displacements in the hexagonal manganites above (first stub column row) and below (second row) the Néel temperature, T_N . The Shannon radii (for eight-coordinated 3+ states) are shown to indicate the radial trend [28].

	Sc	Lu	Yb	Er	Ho	Y
Radius [Å]	0.87	0.977	0.985	1.004	1.015	1.019
						−0.0155(4) ^a [25]
						−0.0125(2) ^a [22]
$T \geq T_N$	−0.0001(72) ^a [22]					
	0.0008(85) ^a [23]	−0.001 ^a [20]	−0.0063(18) ^a [23]	−0.020 ^b [24]	−0.0072(12) ^a [23]	−0.00861 ^a [26]
				−0.005 ^b [12]	0.002(8) ^a [16]	−0.0003(16) ^a [20]
						0.004(8) ^{a,c} [16]
$T \leq 10$ K	−0.0029(16) ^a [23]	−0.003 ^a [20]	−0.0023(19) ^a [23]	—	−0.003(2) ^a [16]	0.0001(7) ^b [27]
					0.0025(86) ^a [23]	0.0089 ^a [20]

^aPowder sample.

^bSingle crystal sample.

^cSample contained oxygen deficiency of 0.29(3) per formula unit. —: No data available.

Since K_3 is the primary order parameter [14], the two coupling strengths β_1 and β_2 are positive and K_1 emerges through its coupling to the K_3 and Γ_2^- modes. These are third-order terms in the Landau free energy, with the form

$$f_{\mathcal{KQP}} = \gamma_1 \mathcal{KQ}^2 \cos(\theta + 2\phi) + \gamma_2 \mathcal{PKQ} \cos(\theta - \phi), \quad (2)$$

which is linear quadratic between K_1 and K_3 and trilinear between Γ_2^- , K_1 , and K_3 . K_1 emerges improperly with $\gamma_{1,2} < 0$. Given the six possible values of ϕ and that \mathcal{P} alternates sign between consecutive values of n [1], Eq. (2) is minimized for $\theta = \pi - 2\phi$ or $\theta = -2\phi$. Thus, the movement of the Mn and apical O sites within the K_1 mode is restricted along the direction defined by ϕ as illustrated in Fig. 1.

In Table I we list reported measured room-temperature and sub- T_N values of δx_{Mn} for six hexagonal manganites. The data illustrate three points. First, δx_{Mn} is small and therefore difficult to quantify, reflected in a spread of reported values. Second, there is no obvious trend in δx_{Mn} across the series. Finally, studies that measure Mn positions above and below T_N report trimers of Mn sites expanding below T_N for YbMnO_3 and YMnO_3 but contracting for ScMnO_3 and LuMnO_3 , with no clear difference for HoMnO_3 . Low-temperature measurements have not been made for ErMnO_3 . These observations lead to three open questions, which we address in this work: First, is δx_{Mn} nonzero? Second, is there a trend in δx_{Mn} across the series? Third, what is the mechanism behind any activation of the K_1 mode, and is it temperature-dependent [20] or temperature-independent [16]?

III. MAGNETO-STRUCTURAL COUPLING

Having described the relevant structural distortions, we now turn to the magnetic properties and thus to the main objective of this study: the coupling between the magnetic order and the crystallographic structure.

A. Magnetic symmetry and properties

The small trigonal-bipyramidal crystal field splitting combined with exchange interaction favors the high-spin state on the formally d^4 , $L=0$ Mn^{3+} ions [5]. These Mn^{3+} mag-

netic moments order at a Néel temperature, $T_N \simeq 70\text{--}90$ K, with higher T_N values corresponding to smaller R -site radii [18,25,29]. The first nearest-neighbor interaction is strongly AFM and geometrically frustrated because of the triangular arrangement of the Mn ions [9].

There are four symmetry-allowed candidate magnetic irreducible representations (irreps), labeled $A_{1,2}$ and $B_{1,2}$, all of which have 120° first nearest-neighbor in-plane configurations. These irreps are generated under the zone boundary magnetic modes mK_2 or mK_3 described by the following respective order parameters: $\mathcal{M}_2 = \mathcal{M}_2(\cos(\psi_2); \sin(\psi_2))$ and $\mathcal{M}_3 = \mathcal{M}_3(\cos(\psi_3); \sin(\psi_3))$ as shown in Fig. 3 [15]. The

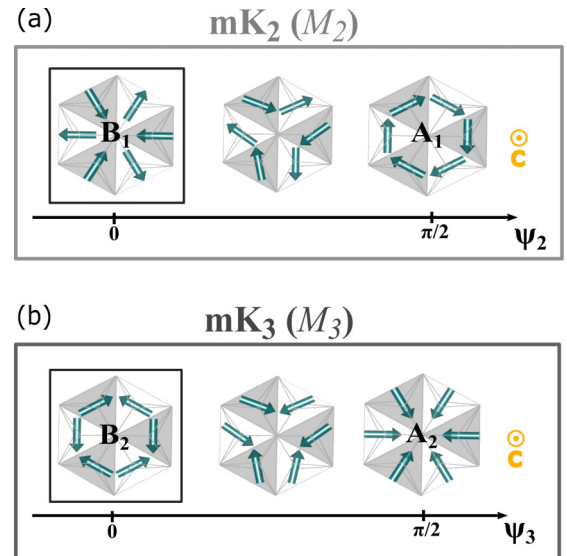


FIG. 3. Planar magnetic configurations associated with the two magnetic modes mK_2 and mK_3 , corresponding to order parameters \mathcal{M}_2 and \mathcal{M}_3 . The magnetic moments on each Mn site are represented by teal arrows. Consecutive planes are colored in different shades. (a) ψ_2 describes the evolution from B_1 ($\psi_2 = 0$) to A_1 ($\psi_2 = \frac{\pi}{2}$) via an out-of-phase rotation of spins belonging to two consecutive planes. (b) ψ_3 describes the evolution from B_2 ($\psi_3 = 0$) to A_2 ($\psi_3 = \frac{\pi}{2}$) via an in-phase rotation of spins belonging to two consecutive planes.

amplitudes $\mathcal{M}_{2,3}$ reflect the amount of correlation of magnetic moments on symmetry-equivalent magnetic sites, and the angles $\psi_{2,3}$ describe the local direction of the Mn magnetic moments as sketched in Figs. 3(a) and 3(b). Within the four irreps, magnetic moments order either radially (A_2 and B_1) or tangentially (A_1 and B_2). The radial irreps A_2 and B_1 also allow for a weak out-of-plane ferromagnetic (FM) and AFM canting, respectively [5,15]. Spins belonging to consecutive layers along the c axis can order with even (A) or odd (B) symmetry under the twofold screw rotation $2\tilde{c}$ [1]. This results in two magnetic moments aligned along the same axis but belonging to consecutive planes pointing either parallel or antiparallel to each other, corresponding respectively to a B- or A-type ordering. All the orders generated under mK_2 and mK_3 would have the same magnetic energy in the high symmetry structure. This energy degeneracy is broken as the structural symmetry is lowered to $P6_3cm$.

B. Coupling between K_3 , Γ_2^- , and $mK_{2,3}$ modes

Magnetic order sets in on the low symmetry structure, and this is expressed by a coupling between the primary order parameter and the magnetic order at fourth order in the Landau free energy expansion of the form [1,5,6,30]

$$f_{Q,M_{2,3}} \propto \mathcal{M}_{2,3}^2 Q^2 \cos^2(2\phi - 2\psi_{2,3}). \quad (3)$$

As a consequence of this coupling, there are two types of in-plane nearest-neighbor interactions: those between two Mn ions that share a trimerization center ($J_{\text{same trimer (st)}}$) (solid gray lines in Fig. 4) and those occupying neighboring trimerization centers ($J_{\text{different trimer (dt)}}$) (solid black lines in Fig. 4). The low symmetry $P6_3cm$ structure also has two different interplanar second nearest-neighbor exchanges, J_{1z} and J_{2z} . A total of six second nearest-neighbors interact with each given site i either via J_{1z} or J_{2z} , the former mediated by two equivalent (both gray in Fig. 4) R sites and the latter by two nonequivalent (one gray and one teal in Fig. 4) R sites. Finally, trigonal bipyramids have easy-plane single-ion anisotropy (SIA), with the hard axis tilted away from the c direction by the K_3 mode. Note that, for a fixed δx_{Mn} , we calculate that the magnitudes of the Γ_2^- and K_3 modes are not influenced by different magnetic orders (see Table S1 in the Supplemental Material [31] for amplitudes of the Γ_2^- and K_3 modes for different magnetic orders). Therefore we can conclude that $mK_{i=2,3}$ do not affect the values of $\gamma_{1,2}$ (defined in Eq. (2)) and that the magnetic order couples only to K_3 through Eq. (3).

Measurement of the exact magnetic ground state in the hexagonal manganites via scattering techniques is complicated by the issue of homometry [15]; magnetic symmetries obtained within one of the $mK_{i=1,2}$ modes lead to near equality of their magnetic structure factors in scattering data if $\delta x_{Mn} = 0$ [15,21]. This is because the high symmetry position of the Mn sites [at Wyckoff position ($x \simeq \frac{1}{3}, 0, 0$), corresponding to $\delta x_{Mn} \simeq 0$] lies in a mirror plane, m_{\perp} [120] [16]. One way to address this issue is by using polarized neutron scattering [27], since the polarized character of the incident beam allows the different ψ_2 and ψ_3 values to be distinguished, or second harmonic generation techniques [9], which are directly sensitive to the symmetry. B_1 and B_2 configurations (framed in black in Fig. 3) have been observed for different members

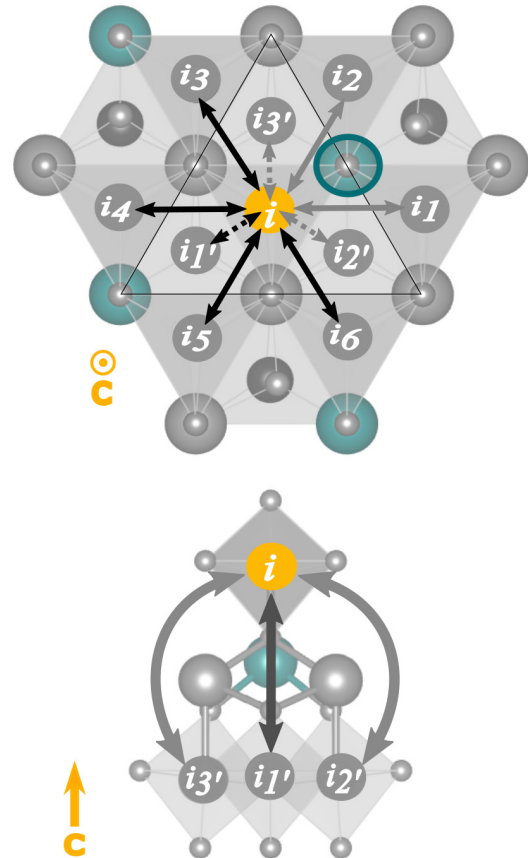


FIG. 4. Symmetric exchanges of a magnetic site i (orange) in the low symmetry $P6_3cm$ structure. Teal R sites indicate trimerization centers (the trimerization center of site i , above and to its right, has a darkened border); nearest-neighbor sites i_1 and i_2 occupy the same trimer as site i , whereas sites i_3 , i_4 , i_5 , and i_6 occupy different trimers. Solid gray and black lines represent same trimer (J_{st}) and different trimer (J_{dt}) nearest-neighbor exchanges, respectively. Dashed black and gray lines represent the interplanar J_{1z} (with site $i_{1'}$) and J_{2z} (with sites $i_{2'}$ and $i_{3'}$), respectively.

of the series using optical second harmonic spectroscopy, with no evidence of A-type order [9].

C. Coupling between K_1 and $mK_{2,3}$ modes

Next, we review the experimental evidence for a sub- T_N δx_{Mn} structural distortion that motivates our investigation of a K_1 - $mK_{2,3}$ coupling [18,20,21]. In $YMnO_3$, powder diffraction measurements indicate that the experimental crystal volume deviates from the Einstein-Grüneisen volume predicted for a nonmagnetic system [21,32]. Additionally, resonant ultrasound spectroscopy detects an elastic stiffening in $YMnO_3$ as the crystal is cooled through T_N [18]. Both experimental techniques show that lattice strain scales with the square of the magnetic order parameter [18,21]. The measured onset of this strain slightly above T_N [18] alludes to a magneto-structural coupling that coincides with the emergence of short-range correlations between spins.

We will now motivate the K_1 - $mK_{2,3}$ coupling using symmetry arguments. The lowest order magneto-structural coupling term that appears in the Landau free energy expansion

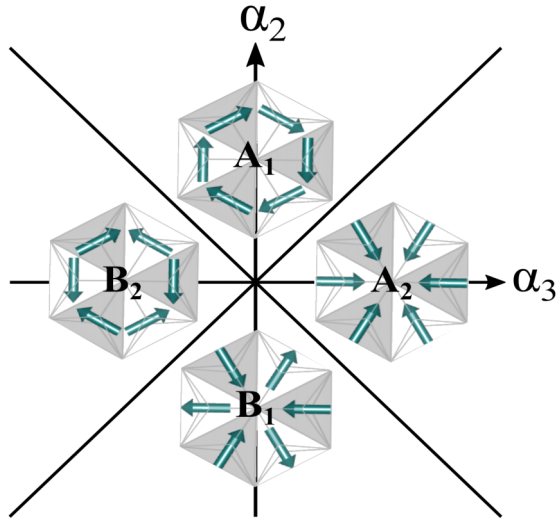


FIG. 5. Magnetic ground state in the phase space of the K_1 - $mK_{2,3}$ coupling parameters $\alpha_{2,3}$. Diagonal lines indicate $|\alpha_2| = |\alpha_3|$.

sion and that remains invariant under the symmetry operations of the $P6_3/mmc$ phase is at third order between the K_1 and the $mK_{2,3}$ modes:

$$f_{K,M_{2,3}} = \alpha_2 \mathcal{K} \mathcal{M}_2^2 \cos(\theta + 2\psi_2) + \alpha_3 \mathcal{K} \mathcal{M}_3^2 \cos(\theta + 2\psi_3), \quad (4)$$

where $\alpha_{2,3}$ are the coupling strengths. For a given K_1 displacement direction θ , these coupling terms are minimized for $i = 2, 3$, by solving

$$\left. \frac{\partial f_{K,M_{2,3}}}{\partial \psi_i} \right|_{\theta, \phi} = 0 \Rightarrow -2\alpha_i \mathcal{K} \mathcal{M}_i^2 \sin(\theta + 2\psi_i) = 0. \quad (5)$$

Using Eq. (5), we calculate the ground-state magnetic phase diagram in the phase space of the two K_1 - mK_2 and K_1 - mK_3 coupling parameters (α_2 and α_3), shown in Fig. 5.

D. Model magnetic Hamiltonian

Next, in order to gain a microscopic understanding of the dependence of the magnetic ordering on the K_1 mode, we write a model Hamiltonian and calculate the interaction parameters as a function of the size and orientation of \mathbf{K} . We describe the energy of the magnetic moment on site i using the following Hamiltonian:

$$\mathcal{H}_i = \hat{e}_i \cdot \left(\underbrace{J_{st} \sum_{j=1,2} \hat{e}_j + J_{dt} \sum_{j=3,4,5,6} \hat{e}_j}_{\text{1st nearest-neighbor exchange}} \right) \quad (6)$$

$$+ \hat{e}_i \cdot 2 \left(\underbrace{J_{1z} \hat{e}_{i1'} + J_{2z} \sum_{j'=2',3'} \hat{e}_{ij'}}_{\text{2nd nearest-neighbor exchange}} \right) \quad (7)$$

$$+ A \cos^2(\psi_{2,3}^i). \quad (8)$$

SIA

Here $\hat{e}_i = (e_i^x, e_i^y, e_i^z)$ is the normalized magnetic moment of a site i where $i = 1, \dots, 6$ designates one of the six magnetic sites of the unit cell and the indices i_j and $i_{j'}$ run over the first and second nearest neighbors of site i , respectively, as sketched in Fig. 4. The nearest-neighbor coupling (mediated by the J_{st} and J_{dt} interactions) contribute equally to the energy in all four magnetic configurations, as can be seen by the 120° arrangement between nearest-neighbor sites in Fig. 3. The difference in energy between the A- and B-type configurations results from the interplanar ordering and is described by the second term of \mathcal{H}_i , where J_{1z} and J_{2z} are the interplanar exchanges illustrated in Fig. 3. The third term (8) gives the in-plane SIA, where A is defined as the energy difference between a spin pointing towards its trimerization center (local x axis) and perpendicular to it (local y axis); $\psi_{2,3}^i$ is the angle describing the magnetic order within the two magnetic modes $mK_{2,3}$ following the description in Figs. 3(a) and 3(b) and projected onto the Mn site's local coordinate system. Since the out-of-plane canting is known to be small we neglect any contribution to the total energy from rotation into the hard axis (see the Methods section for further details).

Taking advantage of the fact that on a frustrated triangular lattice $\hat{e}_{i2'} + \hat{e}_{i3'} = -\hat{e}_{i1'}$, the interactions lifting the magnetic energy degeneracy between A_1 , A_2 , B_1 , and B_2 can be reduced to an effective interplanar exchange term $J_z = J_{1z} - J_{2z}$ and an effective in-plane anisotropy term A . Thus, we obtain the following single-spin Hamiltonian, reduced to only two relevant interactions, J_z and A , in which the first-nearest-neighbor AFM contributions have been absorbed into \mathcal{H}_0 :

$$\mathcal{H}_i = \hat{e}_i \cdot 2 \left[J_{1z} \hat{e}_{i1'} + J_{2z} \underbrace{(\hat{e}_{i2'} + \hat{e}_{i3'})}_{=-\hat{e}_{i1'}} \right] + A \cos^2(\psi_{2,3}^i) + \mathcal{H}_0 \quad (9)$$

$$= 2J_z \hat{e}_i \cdot \hat{e}_{i1'} + A \cos^2(\psi_{2,3}^i) + \mathcal{H}_0. \quad (10)$$

Within this model, the energy, E_i , of each spin \hat{e}_i for each of the four allowed in-plane magnetic configurations is given by

$$E_i(A_1) = -2J_z + \mathcal{H}_0, \quad (11)$$

$$E_i(A_2) = -2J_z + A + \mathcal{H}_0, \quad (12)$$

$$E_i(B_1) = 2J_z + A + \mathcal{H}_0 \quad \text{and} \quad (13)$$

$$E_i(B_2) = 2J_z + \mathcal{H}_0. \quad (14)$$

IV. METHODS

Total energies are obtained within DFT [33] based on the projector augmented-wave method [34] as implemented in the Vienna Ab initio Simulation Package (VASP 5.4.4) [35–38]. Calculations are performed using the Perdew-Burke-Ernzerhof (PBE) generalized gradient approximation [39] combined with an on-site Coulomb repulsion of $U = 4$ eV [5] and an exchange parameter of $J = 1$ eV (following the Liechtenstein approach [40]) on the Mn sites [5,41]. We use the Y_sv, Er_3, Lu, Mn, and O VASP library pseudopotentials.

tials, with $4d$, $5p$, $5p$, and p electrons in the valence band, respectively. We compare the computed $E(B_2) - E(B_1)$ energy difference with calculated values obtained via a different approximation, the local density density approximation with the Ceperley-Alder functional [45,46], and find that the energy trend stays the same, albeit with an energy difference of $\simeq 0.2$ meV. The effects of the U and J values on the computed energies are also evaluated: there is no notable difference between $U = 4$ and $U = 6$, while $E(B_2) - E(B_1)$ presents a steeper energy trend for $J = 1$ than for $J = 0$ with a maximal difference at big negative δx_{Mn} displacements of the order of 0.1 meV. The trends thus seem robust to our choice of U and J as well as our choice of pseudopotential. Finally, we use a cutoff of 700 eV and a gamma-centered k-point grid of $6 \times 6 \times 3$.

Geometries corresponding to the different values of the K_1 mode are obtained by selective dynamics relaxation of the cell, in which the Mn ions are fixed at positions away from their $K_1 = 0$ high symmetry position and the other atomic positions as well as lattice parameters are relaxed. Note that K_1 does not change the cell's symmetry, and the generated geometries remain $P6_3cm$. Within selective dynamics, the $\frac{\epsilon}{a}$ ratio decreases quadratically and symmetrically around $\delta x_{\text{Mn}} = 0$ as Mn ions breathe inwards or outwards. This lattice ratio decreases by $\simeq 0.002$ for the computed compounds as Mn ions shift by $0.01 \times a$ from their high symmetry position. Note that, although K_1 is the only mode that allows a planar movement of Mn ions, the control of K_1 by a constraint on Mn positions within selective dynamics is not perfect. We extract mode amplitudes using the AMPLIMODES software [42,43]. For example, the $\delta x_{\text{Mn}} = 0$ geometry still allows for very small displacements of O_{ap} within K_1 , and Γ_2^- and K_3 are activated, as they couple to K_1 , when the amplitude of K is increased. However, the effect of these couplings is relatively small and will be the object of future works. For simplicity, we use the terms K_1 amplitude and δx_{Mn} interchangeably in this work. Important to note is that, even though Mn ions also relax to $\delta x_{\text{Mn}} \simeq 0$ in the fully relaxed geometries, the latter and the selective dynamics $\delta x_{\text{Mn}} = 0$ structures differ across the three compounds. The fully relaxed geometries have higher $\frac{\epsilon}{a}$ ratios, relative to their selective dynamics relaxed counterparts at $\delta x_{\text{Mn}} = 0$, namely, 1.8788, 1.8654, and 1.8726 compared to 1.8900, 1.8654, and 1.8579 for LuMnO_3 , ErMnO_3 , and YMnO_3 , respectively. Compared to the $\delta x_{\text{Mn}} = 0$ structure, the fully relaxed geometries have higher displacements corresponding to Γ_1^+ and K_3 (by $\simeq 0.01$ and $\simeq 0.015$ Å respectively), as well as lower Γ_2^- displacements (by $\simeq 0.002$ Å). However, the K_1 mode amplitude is similarly small in both geometries. These structural differences are important to keep in mind when comparing the results for the fully relaxed and $\delta x_{\text{Mn}} = 0$ geometries.

A complete description of the SIA can be expressed through the τ_i matrix that is of the following form in each magnetic site's local coordinate system (defined for each Mn site with the local x axis pointing towards the trimerization center):

$$\tau_i = \begin{pmatrix} A_{xx} & 0 & A_{xz} \simeq 0 \\ 0 & A_{yy} & 0 \\ A_{xz} \simeq 0 & 0 & A_{zz} \end{pmatrix}. \quad (15)$$

We find that the weak out-of-plane canting, allowed in the A_2 and B_1 configurations [5], contributes negligibly to the total magnetic energy: the computed values border on the limit of the numerical precision of our DFT computations (10^{-3} to 10^{-4} meV). DFT computed out-of-plane cantings as well as their contributions to the total energy through the DM interaction and SIA can be found in Fig. S1 and Tables S2, S3, and S4 in the Supplemental Material [31]. As a consequence, we do not include A_{zz} and DM interactions in our model Hamiltonian and absorb A_{xx} and A_{yy} into the factor A defined in Eq. (8): $A = A_{xx} - A_{yy}$.

Next, we describe how we compute the Hamiltonian parameters in Eq. (10), following a slightly modified approach from the Four State method developed by Xiang *et al.* [44]. From Eqs. (19) and (20), we see that the J_z values can be obtained by subtracting the energy of configuration A_2 (A_1) from that of B_1 (B_2). We take the J_z value that is the average of the result from the two calculations [as shown in Eq. (18)]:

$$J_z = \frac{1}{4}[E_i(B_1) - E_i(A_2)] \quad (16)$$

$$= \frac{1}{4}[E_i(B_2) - E_i(A_1)] \quad (17)$$

$$\Rightarrow J_z = \frac{(16) + (17)}{2}. \quad (18)$$

Similarly, the A parameters are obtained by subtracting the energy of the A_1 (B_1) configuration from that of A_2 (B_2), and we take the average:

$$A = E_i(A_2) - E_i(A_1), \quad (19)$$

$$= E_i(B_1) - E_i(B_2) \quad (20)$$

$$\Rightarrow A = \frac{(19) + (20)}{2}. \quad (21)$$

We then recalculate A and J_z for a range of δx_{Mn} values and make a linear fit of their dependence on δx_{Mn} using a least squares method. The magnetic energies as a function of K_1 for different magnetic orders are obtained by substituting the A and J_z parameters into the Hamiltonian of Eq. (10). We verify the accuracy of our model and the extracted parameters by comparing our model magnetic energy trends following Eq. (10) with DFT calculated energies. The former are represented by solid lines in Fig. 6 and show excellent agreement with our total energy DFT calculations.

V. NUMERICAL RESULTS

We will focus on calculating the magnetic trends for the following three compounds, in order of increasing radius, $R = \text{Lu}$, Er , and Y for which the Shannon radii for the octahedrally coordinated $3+$ ions are given in Table I. We begin by extracting the parameters A and J_z , defined in Eqs. (18) and (21) at K_1 amplitudes $\delta x_{\text{Mn}} = -0.01, -0.005, 0, 0.005, \text{ and } 0.01$, which cover the spread of reported δx_{Mn} values (Table I).

A. Dependence of in-plane anisotropy on K_1 mode

Figure 7(a) shows the calculated total energy change as a function of in-plane spin angle on four different geome-

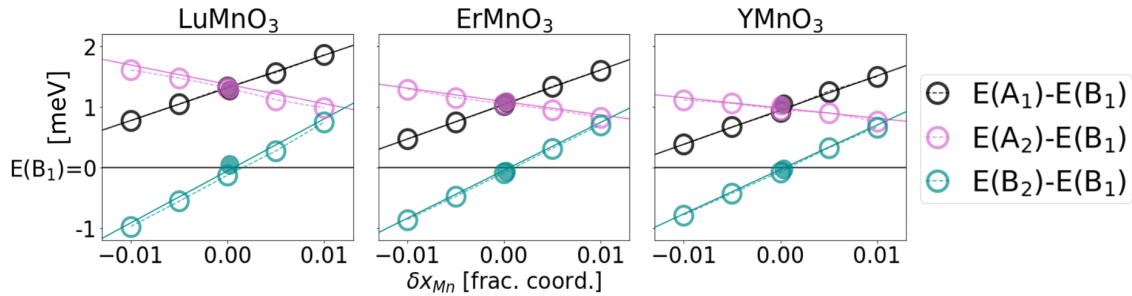


FIG. 6. Total energies of the planar magnetic configurations A_1 , A_2 , and B_2 , relative to the energy of B_1 . Empty circles correspond to DFT calculated total energies for $\delta x_{Mn} \in [-0.01, 0.01]$ fractional coordinates and the dotted lines describe their energy trend. Full lines represent the model Hamiltonian calculated energies. Full circles are DFT total energies calculated on fully relaxed geometries.

tries: a fully relaxed structure and three selective dynamics geometries corresponding to $\delta x_{Mn} = -0.01, 0, 0.01$. Spins located in two consecutive planes are rotated in-phase, so that only the energy contribution of A is varied while keeping the J_z exchange energy constant. Note that this rotation is different from the ones spanning the $mK_{2,3}$ modes in Fig. 7, where both the in-plane anisotropy and interplanar exchange energies change as a function of the rotation. We see that the angle dependence of the total energy E has opposite behavior for $\delta x_{Mn} = -0.01$ and $+0.01$. E has its minimum value (-0.79 meV) for B_2 order ($\psi = n\frac{\pi}{2}$) in the $\delta x_{Mn} = -0.01$ geometry, whereas the B_1 order ($\psi = n\pi$) minimizes E at

0.69 meV) for $\delta x_{Mn} = +0.01$. This indicates that A , as defined by Eq. (20), has opposite values for opposite δx_{Mn} displacements and shows that a linear combination of mK_1 and mK_2 magnetic symmetries is energetically unfavorable. A bigger in-plane anisotropy for $\delta x_{Mn} = -0.01$ than for $\delta x_{Mn} = +0.01$ can be attributed to a bigger K_1 mode displacement in the $\delta x_{Mn} = -0.01$ geometry (by $\simeq 0.0035$ Å). Interestingly, the energy surface flattens for $\delta x_{Mn} = 0$ but not completely as in the fully relaxed structure; the in-plane anisotropy has relatively small local minima at $\psi = n\frac{\pi}{2}$, like in the $\delta x_{Mn} = -0.01$ geometry. These local minima can again be attributed to the imperfect mapping between δx_{Mn} and \mathbf{K} mentioned in the Methods section.

We then calculate A following (21) for all three compounds, as shown in Fig. 7(b) (see Table S5 in the Supplemental Material [31] for more detail on the calculation of A). Importantly, we see that the size of the single-ion anisotropy is similar in all three materials, and that the sign of A changes at approximately $K_1 = 0$ in each case. The sign change indicates a change in the preferred orientation of the spins within the easy plane.

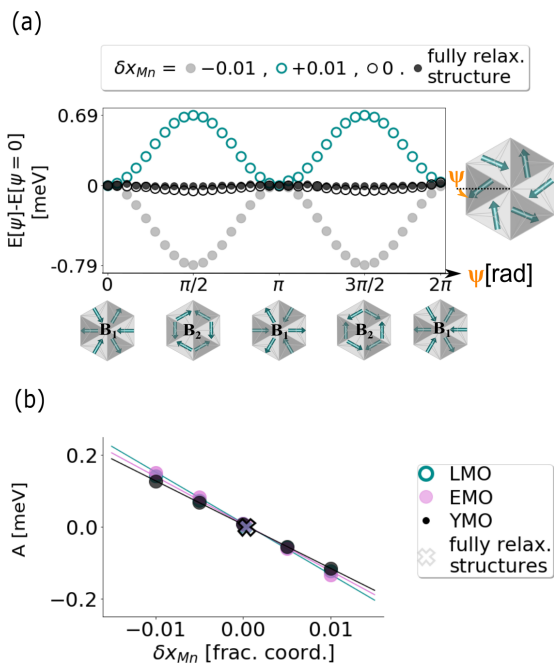


FIG. 7. SIA energy landscape as a function of δx_{Mn} . (a) Total energy of $YMnO_3$ as a function of ψ for three different K_1 geometries ($\delta x_{Mn} = -0.01, +0.01$, and 0) and for a fully relaxed (fully relax.) structure. ψ describes the angle of an in-phase planar rotation of the \mathbf{B}_1 configuration. The in-plane anisotropy A is defined by the energy barrier at the local extrema. A is negative (positive) for $\delta x_{Mn} = -0.01$ ($+0.01$) and is almost nonexistent for $\delta x_{Mn} = 0$. (b) A calculated for $R = Lu, Y$, and Er for a range of δx_{Mn} geometries (circles) and for their fully relaxed geometries (crosses). The full lines represent a linear least squares fit of the DFT calculated energies.

B. Dependence of interplanar exchange on K_1 mode

Next, we analyze the dependence of J_z on the K_1 mode and show the calculated behavior in Fig. 8 (see Table S5 in the Supplemental Material [31] for more detail on the calculation of J_z). Over the range of K_1 values studied, J_z is negative

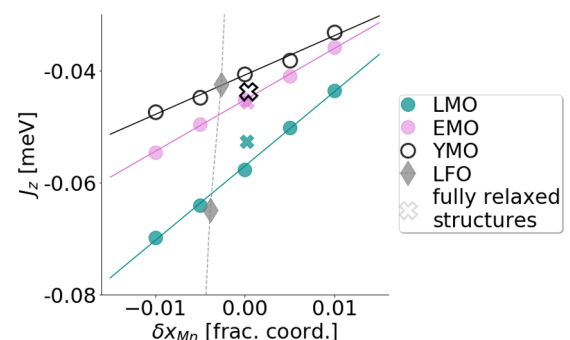


FIG. 8. Circles and crosses represent J_z values calculated in this work using Eq. (18) on $\delta x_{Mn} \in [-0.01, 0.01]$ and fully relaxed geometries, respectively. Gray diamonds connected by dotted lines show results for $LuFeO_3$ from Ref. [41].

for all three materials. This corresponds to an FM (B-type) interplanar interaction, with a linear dependence on K_1 consistent with the configurations observed in second harmonic generation measurements [9]. As the Mn ions shift away from their trimerization centers, their apical oxygens shift by a smaller amount, leading to a decrease in the O_{ap} -Mn orbital overlap and thus to a weaker interplanar FM interaction. The displacement of the apical oxygens within the K_1 mode is similar across the three compounds, explaining the similarity in their $J_z[\text{K}]$ gradient. Additionally, the effective interplanar exchange is stronger for systems with smaller radius R cations and correspondingly bigger trimerization, because J_z reflects the difference between the two different interplanar exchanges. This difference, illustrated in Fig. 4, is larger for bigger bipyramidal tilts. Note that the interplanar exchanges in the fully relaxed structures does not perfectly match the values for the $\delta x_{\text{Mn}} = 0$ geometry. The difference could be due to the slight differences of atomic positions between the two structures mentioned in the Methods section.

For comparison, we show as gray diamonds in Fig. 8 the J_z values extracted for hexagonal LuFeO_3 by Wang *et al.* [41]. Hexagonal LuFeO_3 crystallizes in the same structure as the hexagonal manganites and undergoes an analogous $P6_3/\text{mmc}$ to $P6_3\text{cm}$ structural phase transition. Its B-site chemistry differs from hexagonal manganites in that the Fe^{3+} ions are in a formally d^5 high-spin state. As a consequence of this extra electron, LuFeO_3 has a stronger interplanar interaction [5], and magnetic order sets in at a higher Néel temperature ($\simeq 150$ K). The $J_z[\text{K}]$ trend of LuFeO_3 in Ref. [41] is computed using the LDA+U method with $U = 4.5$ eV and $J = 0.95$ eV. Note that our studies using different choices of functionals (see the Methods section) suggest that this difference in behavior is not a result of small differences in the choice of computational parameters. Figure 8 clearly indicates that a stronger J_z dependence on K_1 such as that found in LuFeO_3 , [41] would be necessary to observe A-type ordering in the manganites [5,41].

C. R-site dependence

We note that the dependence of J_z and A on the size of the K_1 mode is sensitive to the R site, with LuMnO_3 showing the strongest variation and YMnO_3 the smallest. For $-0.015 < \delta x_{\text{Mn}} < +0.015$ the A and J_z parameters span $|A_{\text{max}} - A_{\text{min}}| = (0.43, 0.41, 0.39)$ and $|J_{z,\text{max}} - J_{z,\text{min}}| = (-0.04, -0.03, -0.02)$ for LuMnO_3 , ErMnO_3 , and YMnO_3 , respectively. This trend correlates with the size of the R -site radius, the smallest radius (Lu^{3+}) having the largest polyhedral tilts [7] and in turn the largest change of the magnetic interactions with K_1 . This effect is captured by the first term in the Landau free energy expression (2) in which the K_1 mode amplitude \mathcal{K} is linearly coupled to the square of the K_3 mode amplitude \mathcal{Q} , as well as by the coupling of \mathcal{K} to the squares of the two magnetic order parameters $\mathcal{M}_{1,2}$ in Eq. (4).

D. Ground-state phase diagram

We summarize our calculated parameters and their effect on the magnetic ground state in the phase diagram of Fig. 9,

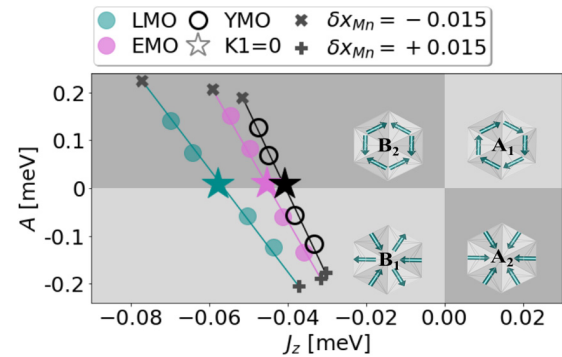


FIG. 9. Magnetic ground-state phase diagram in the model Hamiltonian parameter phase space. Circles represent extracted (J_z, A) pairs, and full lines are linear least-square fits plotted for the range $\delta x_{\text{Mn}} \in [-0.015, 0.015]$, going from top left to bottom right. Points marked by stars are the extracted values for $\delta x_{\text{Mn}} = 0$. Crosses and plus markers indicate parameters for $\delta x_{\text{Mn}} = -0.015$ and $+0.015$, respectively.

where we plot the calculated A as a function of the calculated J_z over the interval $\delta x_{\text{Mn}} \in [-0.015, 0.015]$ for the three compounds. Since magnetic order is known unambiguously, this phase diagram allows us to predict the direction of the manganese displacement for which there is still a large spread in the experimental data. The fact that the B_1 state is measured in YMnO_3 and the B_2 state in ErMnO_3 implies opposite δx_{Mn} displacements in the two materials. The phase diagram also sheds light on the possible origin of spin reorientations observed in some hexagonal manganites. Any change in the spin arrangement could potentially be linked with the change in the Mn position as this creates transitions between A and B type as well as between radial and tangential magnetic orders. For example, the suggested B_2 to B_1 reorientation in LuMnO_3 [9] as temperature decreases could be induced by an Mn displacement from negative to positive δx_{Mn} values. However, Lee *et al.* reported no sign of a corresponding elastic signal [20]. Interestingly, hexagonal LuFeO_3 has a sub- T_N spin reorientation, similarly to LuMnO_3 , but from B_2 to A_2 as the temperature is lowered through 140 K [41]. This translates to not only a change in the sign of A (which is the case in LuMnO_3) but, additionally, to a change in the sign of the interplanar exchange interaction. This crossing from the left (B-type order) to the right (A-type order) part of our phase diagram is attributed to the steeper $J_z[\text{K}]$ trend predicted for LuFeO_3 than for LuMnO_3 in Fig. 8.

Finally, in Table II we summarize the mapping between the A and J_z magnetic Hamiltonian parameters to the K_1 - $\text{mK}_{2,3}$ coupling parameters α_2 and α_3 and to the magnetic ground state. For example, a radial arrangement of spins combined with an AFM interplanar order (A_2) corresponds to a $(A < 0, J_z > 0)$ pair, which is equivalent to the following conditions on the K_1 - $\text{mK}_{2,3}$ coupling parameters: $|\alpha_3| > |\alpha_2|$ and $\alpha_3 > 0$. We have thus managed to describe the magnetic ground state of hexagonal manganites in two different spaces: the phase space of the Landau free energy parameters (α_2, α_3) as well as of the magnetic Hamiltonian parameters (A, J_z) .

TABLE II. Mapping between Landau K_1 -m $K_{2,3}$ coupling parameters (α_2 and α_3), the model Hamiltonian parameters (J_z , A), and the magnetic ground state.

Hamiltonian	Landau	Ground state
$A > 0$ $J_z < 0$	$ \alpha_3 > \alpha_2 $ $\alpha_3 < 0$	\mathbf{B}_2 ($\psi_3 = n\pi$)
$A < 0$ $J_z < 0$	$ \alpha_2 > \alpha_3 $ $\alpha_2 < 0$	\mathbf{B}_1 ($\psi_2 = n\pi$)
$A > 0$ $J_z > 0$	$ \alpha_2 > \alpha_3 $ $\alpha_2 > 0$	\mathbf{A}_1 ($\psi_2 = n\frac{\pi}{2}$)
$A < 0$ $J_z > 0$	$ \alpha_3 > \alpha_2 $ $\alpha_3 > 0$	\mathbf{A}_2 ($\psi_3 = n\frac{\pi}{2}$)

VI. SUMMARY AND OUTLOOK

In summary, this work rationalizes the observed evolution of the magnetic ground state across the hexagonal manganite series and shows that A-type magnetic order is energetically unfavorable as a result of a predominantly inter-planar ferromagnetic interaction [9].

To address the questions prompted by the experimental measurements of the Mn positions presented in Table I, we have determined, using symmetry arguments, the allowed coupling terms for $\delta x_{\text{Mn}} \neq 0$ by extending earlier expansions of the Landau free energy [1,5,14]. The extended Landau expansion reveals a nonlinear coupling of the K_1 mode to

the K_3 and Γ_2^- structural distortions, as well as to the magnetic order parameters. Furthermore, we have shown how $\delta x_{\text{Mn}} \neq 0$ changes the magnetic interactions, using a model magnetic Hamiltonian with DFT-computed parameters, singling out the easy-plane anisotropy and the interplanar symmetric exchange terms as the relevant magnetic interactions that lift the magnetic energy degeneracy between the A_1 , A_2 , B_1 , and B_2 orders. These two findings support experimental measurements of sub- T_N magnetoelasticity [18,20,21] and nonzero, temperature-dependent δx_{Mn} values, and suggest that the K_1 mode is responsible for both. In addition, our calculations indicate that, in materials with smaller R -site radii (and correspondingly larger K_3 distortions), the energy is more sensitive to changes in δx_{Mn} , motivating more precise experimental measurements of this quantity.

Our work indicates that the K_1 mode provides a gateway to controlling the magnetic order in the h- RMnO_3 series by varying its amplitude. We hope that this finding stimulates future studies investigating how the K_1 mode can be modified using external stimuli such as strain or doping.

ACKNOWLEDGMENTS

This work was funded by the European Research Council (ERC) under the European Union's Horizon 2020 research and innovation program project HERO Grant Agreement No. 810451 and by the MARVEL National Center of Competence in Research (NCCR). Computational resources were provided by ETH Zürich and the Swiss National Supercomputing center, Projects No. IDs eth3 and s889.

- [1] S. Artyukhin, K. T. Delaney, N. A. Spaldin, and M. Maxim, Landau theory of topological defects in multiferroic hexagonal manganites, *Nat. Mater.* **13**, 42 (2014).
- [2] Q. N. Meier, M. Lilienblum, S. M. Griffin, K. Conder, E. Pomjakushina, Z. Yan, E. Bourret, D. Meier, F. Lichtenberg, E. K. H. Salje *et al.*, Global Formation of Topological Defects in the Multiferroic Hexagonal Manganites, *Phys. Rev. X* **7**, 041014 (2017).
- [3] S. H. Skjærø, Q. N. Meier, M. Feyngenson, N. A. Spaldin, S. J. Billinge, E. S. Bozin, and S. M. Selbach, Unconventional Continuous Structural Disorder at the Order-Disorder Phase Transition in the Hexagonal Manganites, *Phys. Rev. X* **9**, 031001 (2019).
- [4] Q. N. Meier, A. Stucky, J. Teyssier, S. M. Griffin, D. van der Marel, and N. A. Spaldin, Manifestation of structural Higgs and Goldstone modes in the hexagonal manganites, *Phys. Rev. B* **102**, 014102 (2020).
- [5] H. Das, A. L. Wysocki, Y. Geng, W. Wu, and C. J. Fennie, Bulk magnetoelectricity in the hexagonal manganites and ferrites, *Nat. Commun.* **5**, 2998 (2014).
- [6] M. Giraldo, Q. N. Meier, A. Bortis, D. Nowak, N. A. Spaldin, M. Fiebig, M. C. Weber, and T. Lottermoser, Magnetoelectric coupling of domains, domain walls and vortices in a multiferroic with independent magnetic and electric order, *Nat. Commun.* **12**, 3093 (2021).
- [7] Y. Kumagai, A. A. Belik, M. Lilienblum, N. Leo, M. Fiebig, and N. A. Spaldin, Observation of persistent centrosymmetry in the hexagonal manganite family, *Phys. Rev. B* **85**, 174422 (2012).
- [8] F.-T. Huang, X. Wang, S. M. Griffin, Y. Kumagai, O. Gindele, M.-W. Chu, Y. Horibe, N. A. Spaldin, and S.-W. Cheong, Duality of Topological Defects in Hexagonal Manganites, *Phys. Rev. Lett.* **113**, 267602 (2014).
- [9] M. Fiebig, D. Fröhlich, K. Kohn, S. Leute, T. Lottermoser, V. V. Pavlov, and R. V. Pisarev, Determination of the Magnetic Symmetry of Hexagonal Manganites by Second Harmonic Generation, *Phys. Rev. Lett.* **84**, 5620 (2000).
- [10] J. Oh, M. Le, and H. Nahm, Spontaneous decays of magneto-elastic excitations in non-collinear antiferromagnet (Y, Lu)MnO₃, *Nat. Commun.* **7**, 13146 (2016).
- [11] T. Kim, K. Park, J. C. Leiner, and J.-G. Park, Hybridization and decay of magnetic excitations in two-dimensional triangular lattice antiferromagnets, *J. Phys. Soc. Jpn.* **88**, 081003 (2019).
- [12] B. B. Van Aken, A. Meetsma, and T. T. M. Palstra, Hexagonal ErMnO₃, *Acta Crystallogr. E* **57**, i38 (2001).
- [13] M. Bieringer and J. Greedan, Magnetic structure and spin reorientation transition in ScMnO₃, *J. Solid State Chem.* **143**, 132 (1999).
- [14] C. J. Fennie and K. M. Rabe, Ferroelectric transition in YMnO₃ from first principles, *Phys. Rev. B* **72**, 100103(R) (2005).
- [15] C. J. Howard, B. J. Campbell, H. T. Stokes, M. A. Carpenter, and R. I. Thomson, Crystal and magnetic structures of hexagonal YMnO₃, *Acta Crystallogr. B* **69**, 534 (2013).

- [16] T. Lonkai, D. Hohlwein, J. Ihringer, and W. Prandl, The magnetic structures of YMnO_3 and HoMnO_3 , *Appl. Phys. A* **74**, s843 (2002).
- [17] D. M. Hatch and H. T. Stokes, *INVARIANTS*: program for obtaining a list of invariant polynomials of the order-parameter components associated with irreducible representations of a space group, *J. Appl. Crystallogr.* **36**, 951 (2003).
- [18] R. I. Thomson, T. Chatterji, C. J. Howard, T. T. M. Palstra, and M. A. Carpenter, Elastic anomalies associated with structural and magnetic phase transitions in single crystal hexagonal YMnO_3 , *J. Phys.: Condens. Matter* **26**, 045901 (2014).
- [19] J. Liu, C. Toulouse, P. Rovillain, M. Cazayous, Y. Gallais, M.-A. Measson, N. Lee, S. W. Cheong, and A. Sacuto, Lattice and spin excitations in multiferroic h-YbMnO_3 , *Phys. Rev. B* **86**, 184410 (2012).
- [20] S. Lee, A. Pirogov, M. Kang, K.-H. Jang, M. Yonemura, T. Kamiyama, S.-W. Cheong, F. Gozzo, N. Shin, H. Kimura, Y. Noda, and J.-G. Park, Giant magneto-elastic coupling in multiferroic hexagonal manganites, *Nature (London)* **451**, 805 (2008).
- [21] T. Chatterji, B. Ouladdiaf, P. F. Henry, and D. Bhattacharya, Magnetoelastic effects in multiferroic YMnO_3 , *J. Phys.: Condens. Matter* **24**, 336003 (2012).
- [22] A. Muñoz, J. A. Alonso, M. J. Martínez-Lope, M. T. Casáis, J. L. Martínez, and M. T. Fernández-Díaz, Magnetic structure of hexagonal RMnO_3 ($R = \text{Y, Sc}$): Thermal evolution from neutron powder diffraction data, *Phys. Rev. B* **62**, 9498 (2000).
- [23] X. Fabrèges, S. Petit, I. Mirebeau, S. Pailhès, L. Pinsard, A. Forget, M. T. Fernandez-Diaz, and F. Porcher, Spin-Lattice Coupling, Frustration, and Magnetic Order in Multiferroic RMnO_3 , *Phys. Rev. Lett.* **103**, 067204 (2009).
- [24] P. Liu, X.-L. Wang, Z.-X. Cheng, Y. Du, and H. Kimura, Structural, dielectric, antiferromagnetic, and thermal properties of the frustrated hexagonal $\text{Ho}_{1-x}\text{Er}_x\text{MnO}_3$ manganites, *Phys. Rev. B* **83**, 144404 (2011).
- [25] A. S. Gibbs, K. S. Knight, and P. Lightfoot, High-temperature phase transitions of hexagonal YMnO_3 , *Phys. Rev. B* **83**, 094111 (2011).
- [26] A. K. Singh, S. Patnaik, S. D. Kaushik, and V. Siruguri, Dominance of magnetoelastic coupling in multiferroic hexagonal YMnO_3 , *Phys. Rev. B* **81**, 184406 (2010).
- [27] P. J. Brown and T. Chatterji, Neutron diffraction and polarimetric study of the magnetic and crystal structures of HoMnO_3 and YMnO_3 , *J. Phys.: Condens. Matter* **18**, 10085 (2006).
- [28] R. D. Shannon, Revised effective ionic radii and systematic studies of interatomic distances in halides and chalcogenides, *Acta Crystallogr. A* **32**, 751 (1976).
- [29] B. Lorenz, Hexagonal Manganites-(RMnO_3): Class (I) multiferroics with strong coupling of magnetism and ferroelectricity, *ISRN Condens. Matter Phys.* **2013**, e497073 (2013).
- [30] M. Fiebig, T. Lottermoser, D. Fröhlich, A. V. Goltsev, and R. V. Pisarev, Observation of coupled magnetic and electric domains, *Nature (London)* **419**, 6909 (2002).
- [31] See Supplemental Material at <http://link.aps.org/supplemental/10.1103/PhysRevResearch.4.033204> for extracted mode amplitudes, out-of-plane cantings of the magnetic moments and their contribution to the total energy and more detail on the calculation of J_z and A .
- [32] N. Sharma, A. Das, C. L. Prajapat, and S. S. Meena, Spin reorientation behavior in $\text{YMn}_{1-x}\text{M}_x\text{O}_3$ ($M = \text{Ti, Fe, Ga}$; $x = 0, 0.1$), *J. Magn. Magn. Mater.* **348**, 120 (2013).
- [33] V. I. Anisimov, F. Aryasetiawan, and A. I. Lichtenstein, First-principles calculations of the electronic structure and spectra of strongly correlated systems: The LDA+ U method, *J. Phys.: Condens. Matter* **9**, 767 (1997).
- [34] P. E. Blöchl, Projector augmented-wave method, *Phys. Rev. B* **50**, 17953 (1994).
- [35] G. Kresse and J. Hafner, *Ab initio* molecular dynamics for liquid metals, *Phys. Rev. B* **47**, 558 (1993).
- [36] G. Kresse and J. Hafner, *Ab initio* molecular-dynamics simulation of the liquid-metal–amorphous-semiconductor transition in germanium, *Phys. Rev. B* **49**, 14251 (1994).
- [37] G. Kresse and J. Furthmüller, Efficiency of *ab-initio* total energy calculations for metals and semiconductors using a plane-wave basis set, *Comput. Mater. Sci.* **6**, 15 (1996).
- [38] G. Kresse and J. Furthmüller, Efficient iterative schemes for *ab initio* total-energy calculations using a plane-wave basis set, *Phys. Rev. B* **54**, 11169 (1996).
- [39] J. P. Perdew, K. Burke, and M. Ernzerhof, Generalized Gradient Approximation Made Simple, *Phys. Rev. Lett.* **77**, 3865 (1996).
- [40] A. I. Liechtenstein, V. I. Anisimov, and J. Zaanen, Density-functional theory and strong interactions: Orbital ordering in Mott-Hubbard insulators, *Phys. Rev. B* **52**, R5467 (1995).
- [41] H. Wang, I. V. Solovyev, W. Wang, X. Wang, P. J. Ryan, D. J. Keavney, J.-W. Kim, T. Z. Ward, L. Zhu, J. Shen *et al.*, Structural and electronic origin of the magnetic structures in hexagonal LuFeO_3 , *Phys. Rev. B* **90**, 014436 (2014).
- [42] D. Orobengoa, C. Capillas, M. Aroyo, and J. Perez-Mato, *AMPLIMODES*: Symmetry-mode analysis on the Bilbao Crystallographic Server, *J. Appl. Crystallogr.* **42**, 820 (2009).
- [43] J. Perez-Mato, D. Orobengoa, and M. Aroyo, Mode crystallography of distorted structures, *Acta Cryst. A* **66**, 558 (2010).
- [44] H. Xiang, E. Kan, S. Wei, M. Whangbo, and X. Gong, Predicting the spin-lattice order of frustrated systems from first principles, *Phys. Rev. B* **84**, 224429 (2011).
- [45] D. Ceperley and B. Alder, Ground State of the Electron Gas by a Stochastic Method, *Phys. Rev. Lett.* **45**, 566 (1980).
- [46] J. Perdew and A. Zunger, Self-interaction correction to density-functional approximations for many-electron systems, *Phys. Rev. B* **23**, 5048 (1981).